arXiv:astro-ph/0002469v1 25 Feb 2000

Astrophysical Journal – in press

Revealing the Photodissociation Region: Hubble Space Telescope/NICMOS Imaging of NGC 7027

William B. Latter
SIRTF Science Center, IPAC, California Institute of Technology[1]; latter@ipac.caltech.edu

Aditya Dayal
Infrared Processing and Analysis Center and Jet Propulsion Laboratory[2]; adayal@ipac.caltech.edu

John H. Bieging, Casey Meakin
Steward Observatory, University of Arizona, Tucson, AZ 85721; jbieging@as.arizona.edu; cmeakin@as.arizona.edu

Joseph L. Hora
Harvard–Smithsonian Center for Astrophysics, 60 Garden Street, Cambridge, MA 02138-1516; jhora@cfa.harvard.edu

Douglas M. Kelly
Steward Observatory, University of Arizona, Tucson, AZ 85721, and the University of Wyoming; dkelly@as.arizona.edu

A.G.G.M. Tielens
Kapteyn Astronomical Institute, PO Box 800, NL-9700 AV Groningen, The Netherlands; tielens@astro.rug.nl

ABSTRACT

We report results from a Hubble Space Telescope (HST) and Near-Infrared Camera and Multiobject Spectrometer (NICMOS) program to study the distribution of hot neutral (molecular hydrogen) and ionized circumstellar material in the young planetary nebulae NGC 7027. HST/NICMOS provided very high spatial resolution imaging in line and continuum emission, and the stability and large dynamic range needed for investigating detailed structures in the circumstellar material. We present dramatic new images of NGC 7027 that have led to a new understanding of the structure in this important planetary nebula. The central star is clearly revealed, providing near-infrared fluxes that are used to directly determine the stellar temperature very accurately ($T_\star$ = 198,000 K). It is found that the photodissociation layer as revealed

[1]Mailing address: SIRTF Science Center, California Institute of Technology, MS 314–6, Pasadena, CA 91125

[2]Mailing address: Infrared Processing and Analysis Center, California Institute of Technology, MS 100–22, Pasadena, CA 91125

by near–infrared molecular hydrogen emission is very thin (ΔR $\sim 6\times10^{15}$ cm), and is biconical in shape. The interface region is structured and filamentary, suggesting the existence of hydrodynamic instabilities. We discuss evidence for the presence of one or more highly collimated, off-axis jets that might be present in NGC 7027. The NICMOS data are combined with earlier Hubble Space Telescope data to provide a complete picture of NGC 7027 using the highest spatial resolution data to date. The evolutionary future of NGC 7027 is discussed.

Subject headings: planetary nebulae: general – planetary nebulae: individual (NGC 7027) – ISM: molecules – ISM: structure – molecular processes

1. Introduction

Planetary nebulae have long been thought of as ionized remnants of circumstellar material ejected by stars on the asymptotic giant branch (AGB). That somewhat limited view has changed dramatically, as the neutral component of the remnant circumstellar envelope has been shown to remain observable very late into the lifetime of many planetary nebulae (PNe; e.g., Dinerstein, Sneden, & Uglum 1995; Huggins et al. 1996; Hora, Latter, & Deutsch 1999; and references therein). It is now known that many PNe are characterized by emission from material that is contained in rapidly evolving photodissocation regions (PDRs; Tielens & Hollenbach 1985; Sternberg & Dalgarno 1989; Latter, Walker, & Maloney 1993; Natta & Hollenbach 1998). As the central star and nebula evolve, UV emission from the star increases rapidly. A photodissociation front moves through the gas and slowly turns the mostly molecular nebula to predominantly atomic. At this point, the nebula radiates mainly in the infrared. When the central star becomes hotter than $T_* \approx 30,000$ K, the circumstellar gas quickly becomes ionized and the planetary nebula shines brightly in visible light. The chemical properties of gas in PNe and proto-PNe (PPN) are like those of interstellar PDRs (Latter et al. 1992; Latter, Walker, & Maloney 1993; Tielens 1993; Hora & Latter 1994), which are well modeled (see Hollenbach & Tielens 1997). The time over which molecular material can be present in PNe is typically predicted to be a rather brief period in the lifetime of PNe (e.g., Tielens 1993; Natta & Hollenbach 1998). But, such timescales predicted from current chemical models are limited by observational data and lack of a clear understanding of the morphology and density structure of these objects.

NGC 7027 is perhaps the best studied planetary nebula, in part because of its proximity (about 900 pc; e.g. Masson 1989) and high surface brightness at all wavelengths. It has a very rich atomic and molecular spectrum, making it ripe for study at all wavelengths, and it is rich in physical and chemical information (see, e.g., Graham et al. 1993a; Cox et al. 1997, and references therein). Because of its compact size as viewed from Earth ($\approx 15''$), the morphology, particularly that for the H_2 emission, of this object has been suggested, but has not been clearly revealed (see, e.g., Graham et al. 1993a; Graham et al. 1993b; Kastner et al. 1994; Latter et al. 1995). The

elliptical ionized core lies at the center of an extended molecular envelope (Bieging, Wilner, & Thronson 1991). At the interface between the cold molecular envelope and the hot ionized region is an apparent "quadrupolar" region of strong near–infrared (IR) rotational-vibrational molecular hydrogen emission (Graham et al. 1993a) that has been shown to be excited by absorption of UV photons in the photodissociation region (Hora, Latter, & Deutsch 1999).

A detailed understanding of the morphology of planetary nebulae is important. It has been demonstrated that there is a strong correlation between the presence of molecular emission from PNe and the observed morphology of the PNe, such that objects that contain large amounts of molecular material are bipolar or butterfly nebulae (Hora, Latter, & Deutsch 1999; Kastner et al. 1996; Huggins et al. 1996; Huggins & Healy 1989; Zuckerman & Gatley 1988). Progenitor mass also correlates with morphological type, such that higher mass stars appear to produce bipolar or butterfly nebulae (see Corradi & Schwarz 1994). This correlation suggests that the higher mass AGB progenitors, which probably have the highest mass loss rates, produce dense, long lived molecular envelopes (Hora, Latter, & Deutsch 1999).

The evolution of PDR and PNe, and the correlation between morphology with molecular content are not fully understood. Because NGC 7027 is in a rapid and key moment in evolution (the transition from neutral, predominantly molecular envelope to an ionized one), it is worthy of serious study into its chemical and physical properties and its detailed morphology. The Hubble Space Telescope and NICMOS provided the high spatial resolution, dynamic range, and stable background needed to examine the near-IR nature of NGC 7027. In this paper, we present narrowband images in the $v = 1 \rightarrow 0$ S(1) ($\lambda = 2.121$ μm) line of molecular hydrogen and other filters that trace the ionized core and the nearby neutral region. These images show with unprecedented clarity the true structure of NGC 7027. In Sections 2 and 3, we discuss the data, the apparent morphology, and the presence of a jet (or jets) in the object. In §4 we present a 3-dimensional model for the overall structure, including the photodissociation region. Section 5 presents a discussion of the excitation of the nebula and the central star properties. We then consider our results in light of previous work, and discuss the evolution of the PDR in NGC 7027.

2. Observations and Data Reduction

We have imaged NGC 7027 with the Hubble Space Telescope (HST) and the Near-Infrared Camera Multiobject Spectrometer (NICMOS) at 7 near-infrared wavelengths between 1.1 μm and 2.15 μm (Figs. 1 and 2). The 1.10 μm broadband (F110W) observations were made with Camera 1 (pixel scale = 0.043″ pixel^{-1}, field of view or FOV = 11″×11″). All of the other observations were made with Camera 2 (pixel scale = 0.075″ pixel^{-1}, FOV = 19.2″×19.2″). The observations were made in one of the multiaccum detector readout modes (usually multiaccum 256; see the NICMOS Instrument Handbook) to obtain a very high dynamic range. A variety of dither patterns were utilized to sample the array uniformly; in the case of the F110W observations dithering/mosaicing was required to obtain a complete image of the source. Chop (or blank sky)

frames for background subtraction were also obtained for all filters except F110W and F160W (1.60 μm broadband). From ground-based observations it was known that the full extent of the H_2 emission in NGC 7027 is slightly larger than the NICMOS Camera 2 field of view. A specific orientation of the Observatory was used to put the largest known extent of the emission along a diagonal of the array. Dither patterns were used that would ensure complete coverage of the emission. The method worked very well, and no emission was missed, although it does appear that very low level scattered light does extend off the array in some of the bands observed. A summary of the observations is presented in Table 1, and the data are presented in Figs. 1 and 2.

The data were originally reduced and calibrated by the standard Space Telescope Science Institute (STScI) NICMOS pipeline, but we subsequently re-reduced all of the data using better characterized calibration files (flat-fields, dark frames, and bad pixel masks) as well as a revised version of the STSDAS calibration task calnicA. After reduction of individual frames, the multiple images at each wavelength were mosaiced together using the STSDAS calnicB task in IRAF[3]. The reduced images were flux calibrated using NICMOS photometric calibration tables provided by M. Rieke (private communication). The HST Wide Field/Planetary Camera (WFPC2) data were acquired from the STScI HST data archive.

Isolating the H_2 emission – An examination of the near-IR spectrum of NGC 7027 (Hora, Latter, & Deutsch 1999), and the F212N and F215N filter transmission curves shows that both filters suffer from line contamination. In addition to the H_2 $v = 1 \rightarrow 0$ S(1) line at 2.121 μm, the F212N filter also transmits the 2.113 μm He I line at $\sim 83\%$ of peak transmission. The F215N filter, used for sampling continuum emission adjacent to the H_2 line, includes within the filter bandpass the Brγ line at 2.167 μm at $\approx 2 - 4\%$ transmission. We made use of all available data, theoretical modeling, and empirical fitting to provide the cleanest possible subtraction of the continuum and contaminating lines in the H_2 image. A simple subtraction of the flux calibrated continuum image from the line image not only isolates the H_2 emission but also shows a dark (negative) inner ring-shaped region that resembles the ionized nebula; this inner region is an artifact of over–subtraction of the He I line contribution from the H_2 filter data. Typically, a bright ring of He I emission is seen in ground–based narrowband H_2 images of NGC 7027 (see, e.g., Graham et al. 1993a; Latter et al. 1995; Kastner et al. 1994; Kastner et al. 1996), because the continuum filters most often used do not include Brγ emission in the bandpass.

Since uncertainties associated with filter transmission are largest along the edges of the bandpass (where transmission changes rapidly with wavelength), we first made an estimate of the Brγ transmission. Using the F190N image as "true" continuum for the F215N image, we compared the observed Brγ flux with that obtained by Hora, Latter, & Deutsch 1999 using ground–based spectroscopy. We measured our fluxes at both of the spatial locations at which their slits were

[3]The Image Reduction and Analysis Facility is written and supported by the National Optical Astronomy Observatories (NOAO) in Tucson, AZ

placed (labelled N and NW in their paper) and found that we detect approximately 7 – 8% of their Brγ fluxes at each point. Since the Brγ to He I ratio is $\sim$ 15 (Hora, Latter, & Deutsch 1999) and assuming that the He I line is transmitted at 83% of peak, this implies that we need to scale the F215N image by $\sim$ 0.8 to cancel out the He I emission in the (F212N – F215N) difference image. This process of eliminating line contamination assumes that the the He I to Brγ ratio is fairly constant over the nebula. Photoionization modeling using CLOUDY (Ferland 1997) shows that $S_{HeI}/S_{Br\gamma}$ ratio does not change by more than 20% over the region 1.5×10^{17} cm to the outer edge, 3×10^{17} cm ($\approx$ 10″– 20″). Thus, we can scale the Brγ emission (i.e., the F215N image) to cancel out the He I emission in F212N – F215N difference image to a very high degree. Given the uncertainties involved in this procedure, we used scale factors in the range 0.7 – 1 to determine the best H_2 difference image empirically. We found that a value of 0.9, when applied to the F215N image, provided the cleanest subtraction of the continuum and He I from the F212N image. This scaling factor is consistent with $\sim$ 6% Brγ transmission in the F215N filter. This procedure has resulted in the nearly pure molecular hydrogen emission image of NGC 7027 shown in Figure 3.

The continuum subtracted H_2 image has an integrated line brightness of 3.8×10^{-12} erg s^{-1} cm^{-2} and an average surface brightness of 8×10^{-4} erg s^{-1} cm^{-2} ster^{-1}. Using a similar process of aligning images before subtraction we find an integrated Pα line flux (the F187N line filter and F190N continuum filter; see Fig. 1) of $\approx 5.5\times10^{-10}$ erg s^{-1} cm^{-2}(Fig. 1).

3. General Results

3.1. Observed Nebular Properties

Most of the images (narrow- and broad-band) are remarkably similar (see Figs. 1 and 2). The emission is dominated by a bright, patchy elliptical ring (major axis along PA = 150°) which is the ionized nebula; the overall shape and extent of this nebula is similar to that previously observed in visible light, near-IR, and radio continuum images (e.g., Roelfsema et al. 1991; Woodward et al. 1992; Graham et al. 1993a). Compared to the visible light images of HST/WFPC2 that show a "filled-in" ellipsoid, the near-IR morphology (where optical depths are lower) clearly shows an ellipsoidal shell. The high spatial resolution of these new HST/NICMOS images clearly resolves the ellipsoidal shell into apparent clumps (or "clump-like" variations in brightness), regions of varying surface brightness, and dark dust lanes. The brightest region appears to be a clump located about 4″ NW of the center of the nebula (marked by the location of the visible central star). The central star stands out clearly in the continuum images. The similarity between the Pα and continuum images suggest that the broad-band filters trace free-free or free-bound emission from hot gas, rather than dust-scattered starlight, which is apparent as extended emission in the WFPC2 data. The F212N filter clearly shows a second, spatially distinct component that is not seen in the other filters: wisps of ro-vibrationally excited H_2 emission that appears to surround the ionized nebula. Furthermore, there is also clear evidence of a disruption of the gas along a

NW-SE (PA $\sim$ 130° measured E of N) axis; this might be caused by wind interactions with an off-axis bipolar jet (see §3.2).

The continuum–subtracted H_2 image (Fig. 3) clearly shows two bright intersecting rings, which we interpret as brightened rims of an inclined biconical structure (§4.1). This structure encloses the roughly elliptical ionized region. The structures seen in molecular hydrogen emission and in tracers of the ionized core appear different and spatially distinct.

3.2. A Possible Collimated, Off-axis Jet

The H_2 emission (Figs. 1 – 3) shows bubble-like extensions at the outer edge of the bulk emission region. This apparent disturbance falls along an axis $\approx$ 20°– 40° (PA = 130° NW to SE) to the west of the polar axis, extending through the central star to the opposite side of the nebula (PA = 130° NW to SE). There are hints of these structures in ground-based near–IR data (Graham et al. 1993a; Kastner et al. 1994; Latter et al. 1995) as well as in radio continuum images of the ionized region (Roelfsema et al. 1991). Because of the clarity of these new data, we can now suggest a cause for this structure. The wisps of H_2 emission revealed clearly in these HST data indicate that this region has been disturbed by something other than dust–photon interactions or a uniform, radially directed, outflowing wind. We suggest that there is present in NGC 7027 a highly collimated, "off-axis" jet. The disturbance is not only seen in the molecular region, but is clearly evident in the ionized core along precisely the same position angle. The structure extends into the region of scattered emission seen in the WFPC2 images as well (see also Roelfsema et al. 1991). The sharpness of the extended WFPC2 emission argues against something like turbulent instabilities. There is no kinematical evidence for the jet, nor is there any extended collimated emission in the HST images; this leads us to believe that the jet may have disrupted the nebula in the past and has now died down. At a much lower level, there appears to be similar evidence for another jet, or the same jet precessing, at a polar angle of $\approx$ 10° to the east of the north pole. Along an axis in this direction there is an additional region of "disturbed" H_2 emission most clearly seen on the southern side of the nebula. The ionized core has apparent breaks or disruptions along this axis on the northern side, and extensions can be seen in the WFPC2 data as well (Figs. 2 and 3). The locations of these features are indicated by lines 1 and 2 in Fig. 3.

We speculate that the disturbed morphology of NGC 7027 might be a result of one or more BRETs (bipolar rotating episodic jets; e.g., Lopez et al. 1998). In this regard we note that the two axes that we have identified simply show the most pronounced structure; however much of the other billowy structure and wisps (especially prominent in the H_2 data) is likely caused by the same, or similar processes. Evidence for precessing, collimated jets that are on, or away from the primary PN axis are also seen in a number of other PNe. The most striking example might be NGC 6543 (the "Cat's Eye Nebula;" Lame, Harrington & Borkowski 1997). NGC 7027 appears to be in a very early stage of forming a jet, or perhaps the jet is a transient phenomenon. The fact that we do not see the jet itself suggests that either we have not found the right diagnostic line or

wavelength to probe the jet kinematically, or the jet has now shut off.

4. A 3-dimensional Spatial and Kinematical Model

We have modeled the spatial and kinematical structure of NGC 7027 using a geometrical modeling code described by Dayal et al. (1999). The code uses cartesian coordinates (for adaptability to different geometries), and the nebula is divided into 10^7 $0\farcs075$-sized cells. In these models the nebula is assumed to have azimuthal symmetry with the star at the center. Once the shape and dimensions of a source have been set, the density, temperature, or velocity fields can be specified independently as functions of the radial distance from the center and/or latitude. The expansion of the nebula is assumed to be purely radial, directed away from the central star. The tilt angle of the nebula (w.r.t. the plane of the sky) can be varied independently for each model. Assuming that the emission is optically thin, the code numerically integrates the emission per cell along each line of sight, to produce surface brightness and position–velocity (P–V) maps. The surface–brightness maps are convolved with a gaussian beam (FWHM = $0\farcs25$) to match the instrumental point spread function. The source function, which determines the emission in each cell, can be specified as a function of the local temperature and/or density depending on the emission mechanism that is being modeled (recombination line emission, dust thermal emission, dust scattering etc.).

The physical parameters for the nebular model are well constrained by the high spatial resolution afforded by HST and NICMOS. Ground–based kinematical data that have been obtained with CSHELL at the IRTF provide radial velocity information, which imposes even stronger constraints on the nebula's 3-D structure; these data also provide valuable information on the dynamics and evolutionary timescales of the nebula. A full presentation of these data will be made elsewhere (Kelly et al. 1999) Note that changing the model geometry changes the shape of the image and the P-V diagram; changing the density law changes the relative location and contrast of bright and dark regions in the image and the P-V diagram, but not the shape/size of the image; finally changing the velocity law does not affect the image but changes the shape of the P-V diagram. Therefore, model images together and P-V diagrams, impose strong constraints, allowing us to develop fairly robust models for the spatial and kinematical structure of the source.

We focus here on reconstructing the 3-dimensional structure of the excited H_2 shell, which represents the PDR. However we also construct a model of the Pα emission and compare the density and velocity structure of ionized gas that we derive, with Pα and radio recombination lines respectively, and estimate a total mass for the ionized gas. Finally, we also construct a spherical, isotropically scattering dust model and compare those results with a WFPC2 continuum image. Note that each of the 3 components is modeled separately, using independent constraints provided by different images. We adopt source functions and emission coefficients appropriate for the nebular temperature and density, for each of the three components.

4.1. Excited H_2 – The Photodissociation Region

4.1.1. Geometry

The H_2 emission is modeled as a "capped" bi-conical (hourglass-shaped) structure which shares the same axis, but lies exterior to the ionized nebula (Fig. 4). The outer dimensions of the bi-cone are well constrained by the continuum subtracted H_2 image (Fig. 3): The intersecting outer rings represent the maximum diameter of the cone; the major axis to minor axis ratio constrains the tilt of the cone to be $i \approx 45° \pm 5°$ (w.r.t. the plane of the sky). Based on an established tilt and a maximum cone diameter, the observed separation between the large rings determines the height of the cone. The radius of the waist of the hourglass is harder to constrain from the data due to projection effects. We simply assume that this dimension matches the minor axis of the ionized gas ellipsoid (§4.2), $R_w = 2\farcs8$, though in reality, the neutral gas probably lies somewhat outside the ionized gas. The waist diameter along with the maximum diameter of the cone allows us to estimate an opening angle for the cone. There is some evidence in the images that the H_2 emission is not confined to a conical shell that is open at the poles, but extends all around the ionized gas ellipsoid. Wisps of H_2 emission are seen superposed on the northern and south-eastern parts of the ionized nebula in Fig. 2. Also, our model images show that an "open" cone cannot produce the bright rims, along the top and bottom of the structure, as are seen in the images. When a "cap" of similar thickness as the walls of the bicone is added, limb brightening along lines of sight through the caps alleviates this problem (see Figs. 5(a),(b)). By comparing intensity cuts across the model with similar cuts across the image we more accurately determine the dimensions of the H_2 shell. The walls of the bicone are constrained by the thickness of the observed H_2 rims, $\Delta R \sim 0\farcs5 \pm 0\farcs1$ ($6 \pm 1 \times 10^{15}$ cm at the adopted distance of 0.88 kpc). For example, increasing the width of the shell reduces the gap between the rims of the H_2 bicone and the inner, ionized gas ellipsoid; decreasing the width of the shell produces narrower looking rims than are seen in the NICMOS-only color composite image (Fig. 2(a)). Because the nebula is inclined to the line of sight, it is difficult to ascertain variations in the thickness of the H_2 shell as a function of latitude (particularly at low latitudes). We assume therefore that the shell has a constant width.

Limitations – The cone/cap model here is an approximation to the nebula, which probably has a smoother, bi–lobed shape. However, building up the model in separate components allows us to see the effects of the cap (or lack thereof) on the P-V diagram and images. Though we do not believe that a smoother hourglass figure model would yield significantly different results, it may match the brightness in the interior (equatorial regions) of the H_2 images somewhat better than our current models, which appear to overestimate the H_2 brightness in this region.

4.1.2. Kinematics

Long-slit CSHELL spectra of the H_2 $v = 1 \rightarrow 0$ S(1) line are invaluable in constraining the geometry of the source more tightly. The P-V diagram obtained by placing the slit along the major axis of the source is shown in Fig. 6. The emission region has an elongated elliptical shape suggesting that there are distinct red and blue–shifted components of emission both in the top and bottom halves of the nebula. The shape of the P-V diagram confirms that the nebula is oriented such that the N-E part of the shell is tilted *towards* the observer and the S-W part is tilted *away* from the observer. This orientation is consistent with that of the ionized gas ellipsoid observed by Bains et al. 1997, who used an echelle spectrograph with a velocity resolution of 6 km s^{-1}. The four bright "spots" of emission, located symmetrically about the center of the nebula, indicate locally bright regions along the slit separated in velocity. The two bright regions closer to the center mark the position of the limb–brightened inner rims of the bicone on the slit, while the bright regions at the top and bottom correspond to the limb-brightened "caps" of the bicone, which lie almost in the plane of the sky. It is the position-velocity diagram that uniquely constrains the distribution of H_2 along the poles. Figs. 5 (c) and (d) show model P-V diagrams obtained with and without a cap. Clearly a conical structure *with* the spherical cap gives a more complete fit to the observed P-V diagram than one without the cap. A constant expansion velocity of 20 km s^{-1} is able to reproduce the observed spectra quite well though we cannot rule out deviations from this law on smaller spatial scales. Figs. 6 (b), (c) show how the shape of the model P-V diagram changes with the velocity law. In general, a larger velocity law exponent results in a larger "kink" in the position velocity diagram, corresponding to more abrupt change in the projected velocity from the rim of the cone (large R) to the interior of the cone. A comparison with the data allows us to rule out a velocity exponent, $\alpha \geq 1$. Thus, for our adopted model geometry we can rule out a constant dynamical timescale for all points in the H_2 shell, as one might expect for an aspherical shell expanding in a self-similar way. The velocity law implies that at a latitude of 25° the walls have a dynamical timescale of 950 yr and further out, at 36° (where the bicone ends and the spherical cap begins) the timescale is $\sim$ 1,300 yr. We note that since this is an expanding photodissociation front, the dynamical timescale is not the most appropriate one for characterizing the evolution (see §6.2).

4.1.3. Density

Though the excitation of H_2 is primarily via absorption of UV photons (i.e. non-thermal, see §5.2) we assume here that the H_2 is thermally excited and that the level populations are described by a vibrational excitation temperature in the range $T_{vib} \approx 6,000 - 9,000$ K (see Hora, Latter, & Deutsch 1999). Later in this paper we show that this assumption gives reasonable results when compared to more detailed models of dense PDRs. If the H_2 emission is optically thin, then the model intensity at each pixel is simply proportional to the density of H_2 molecules integrated

along a given line of sight:

$$\epsilon_{H_2} = \int j_{H_2} n_{H_2}\, dl \tag{1}$$

where the emission coefficient (in erg s^{-1} cm^{-2} per molecule) is

$$\epsilon_{H_2} = \frac{A_{u,l} g_N (2J+1) h\nu}{4\pi Q(T) e^{\frac{E_u}{T}}} \tag{2}$$

and *dl* is the spatial increment along the line of sight. The spontaneous radiative decay coefficient for the 1–0 S(1) line, $A_{u,l} = 3.47{\times}10^{-7}$ s^{-1} (Wolniewiez, Simbotin & Dalgarno 1998), the nuclear spin statistical weight $g_N = 3$ (ortho-H_2) and J=3. The energy of the upper level of the transition, $E_u = 6947$ K. Using the polynomial coefficients for the partition function, $Q(T)$, given in Sauval & Tatum 1984 we calculate the change in the product, $\delta \equiv Q(T)\ e^{\frac{E_u}{T}}$ with temperature in the range 2000 K $\leq$ T $\leq$ 11,000 K. We find that δ changes by about a factor of 1.5 over the range 6,000 $\leq$ T $\leq$ 9,000 K. We simply assume $\delta = 220$, and use this in the the above equation.

Using the equation above to fit the observed integrated intensity of H_2 ($3.8{\times}10^{-12}$ erg s^{-1} cm^{-2}; §3.1.1) and the H_2 radial brightness profile (Fig. 7(a)) allows us to estimate an *excited* H_2 density of $n \sim$ 10–13 cm^{-3} (depending upon the poorly known attenuation value) for a filling factor of unity. Summing over the entire nebula then yields a total mass of $M_{ex} \approx 10^{-5}$ $M_\odot$ for the excited H_2. A constant density H_2 law provides adequate fits to the images and the P-V diagrams.

4.2. Ionized Gas Emission and Scattered Starlight

Pα emission – The ionized nebula is well reproduced by a prolate ellipsoidal shell, as has been shown previously (Atherton et al. 1979; Roelfsema et al. 1991). Using the inclination of 45° estimated from the H_2 image, we calculate the lengths of the semi–major and semi–minor axes (a_y and a_x in Fig. 4). The thickness of the shell (though it has a broken, patchy appearance) is estimated to be about $0\farcs9$ ($1.2{\times}10^{16}$ cm), from the radial cuts taken in orthogonal directions through the walls (see Table 2). Ignoring the contribution of electrons from heavier elements (i.e. assuming $n_e = n_H$), the model surface brightness in Pα is given by:

$$I_{P\alpha} = \int j_{P\alpha} n_e^2\, dl \tag{3}$$

where $j_{P\alpha}$ (Pα emission coefficient) = $3.27{\times}10^{-27}$ erg cm^3 s^{-1} $ster^{-1}$ assuming case B recombination, $T_e = 10^4$ K (Table 4.4; Osterbrock 1989) and l is the path length through the nebula at any given position on the projected surface of the nebula.

The density law for the ionized gas is constrained by comparing the model image (and radial cuts) with the Pα image, although the clumpy nature of the ionized shell makes it somewhat difficult to fit a well–defined power law. Our results indicate that models with a constant density or slowly decreasing radial power laws ($R^{-\alpha}$, $0 \leq \alpha \lesssim 0.5$) models provides an adequate fit to the

data (Figs. 7(b)). In models with $\alpha \geq 1$ the polar densities are considerably lower than those along the equator (Figs. 8(c),(e)); consequently radial cuts along the poles show a smaller rise in intensity going from the center outwards, than do radial cuts along the equator. The cuts through the observed image clearly do not show such a difference between the orthogonal radial cuts.

We are able to match the observed Pα image with a constant density model where the density in the shell is $n_{H^+} = 6{\times}10^4$ cm^{-3}. We also impose an upper limit to the density inside the ellipsoidal shell, $n_{e,interior} \leq 5{\times}10^3$ cm^{-3}. These densities, together with the derived geometry imply that the total ionized mass is $M_{ion} \sim 0.018$ M$_\odot$. (The mass might be about 50% higher if the attenuation factor is, $A_V = 2.97$ mag – see Section 5.1). This low density inner cavity implies high temperatures ($\gtrsim 1 \times 10^5$ K), possibly shock heated in interacting winds. This suggests that diffuse X-ray emission from a hot gas might be detectable from NGC 7027, in addition to point source X-ray emission from the central star.

Our derived shell density agrees very well with the density derived by Roelfsema et al. (1991; $6{\pm}0.6 \times 10^4$ cm^{-3}) from radio continuum observations. We are unable to reproduce the total ionized mass of 0.05 M$_\odot$ that they infer, given their ellipsoid dimensions and density (at an assumed distance of 1 kpc). Using their parameters we find an ionized mass, $M_i \sim 0.025$ M$_\odot$. The PV diagrams presented in Fig. 8 (which assume that velocity is constant) are consistent with that presented for ionized gas by Roelfsema et al. 1991. A careful examination of the intensity contrast in the constant–density model suggests that this model most closely matches these data, given the S/N of the data.

Dust scattering – An examination of the WFPC2 F555W image of NGC 7027 shows that the ionized nebula is surrounded by an extended region of lower surface brightness. The radial profiles indicate that the intensity falls off as I $\propto$ R^{-3}, the expected index for singly scattered starlight from an optically thin region of the dust shell. We model the scattered starlight as single (isotropic) scattering from a spherical shell of 0.1 μm sized amorphous carbon grains, with a scattering cross-section, $K_s = 8{\times}10^4$ cm^2 gm^{-1} at 0.55 μm (Martin & Rogers 1987). The photon source is assumed to be a 200,000 K black-body. Assuming an AGB dust mass loss rate of 10^{-6} M$_\odot$ yr^{-1} and an expansion velocity of 10 km s^{-1} yields a model flux density of $\sim 4.6{\times}10^{-4}$ Jy arcsec^{-2} at a distance of $5''$ from the center of the nebula. The model radial brightness profile appears to match the observed surface brightness in the F555W image, along the minor axis of the nebula (Fig. 7c). The dust mass loss rate agrees well with the gas mass loss rate of $1.5{\times}10^{-4}$ M$_\odot$ derived by Jaminet et al. 1991 if the gas to dust ratio is ~ 150.

We have tried to fit the broad–band near–IR emission with the same scattering model as used above for the WFPC2 image. We find that assuming $\sigma_s \sim \lambda^{-4}$ (Rayleigh scattering, appropriate for small grains) yields near–IR intensities that are considerably lower than those observed in the F160W and F205W filters. A better estimate is obtained if the scattering cross–sections goes as λ^{-1}, implying that the dust scattering is dominated by larger ("fluffy") grains. Also, the

radial profiles in the near-IR filters do not show a well–defined radial power law as seen in the WFPC2 image, suggesting that the optically thin, singly scattered starlight model is inadequate in describing the extended near-IR emission. We suspect that the emission in the near–IR broad–band filters is not simply scattered starlight but includes scattered line/f-f emission as well as possibly some dust thermal emission. A quantitative description of this "excess" near–IR emission will require a detailed model of the gas and dust emission and is not addressed further this paper.

5. Central Star and Nebular Excitation

5.1. Properties of the Central Star

The central star (CS) of NGC 7027 has been detected only with difficulty from the ground at visible wavelengths and under average seeing, because of the low contrast of the star relative to the bright nebular emission (Jacoby 1988; Heap and Hintzen 1990). NICMOS offers high resolution imaging at longer wavelengths where extinction from interstellar and circumstellar dust is much smaller than at visible wavelengths, and the contrast of the stellar point source is greatly enhanced by the high angular resolution of HST. This observational advantage allows a significant improvement in photometric data for the CS and in the stellar properties thereby inferred.

Photometry for the CS was obtained for the F110W, F160W, F190N, and F205W NICMOS filters. We have also determined CS fluxes for the F555W and F814W filters of the WFPC2 optical camera, from images in the HST data archive. Nebular photometry of the Pα and H_2 $v = 1 \rightarrow 0$ S(1) line emission was derived from the line and continuum filter sets, F187N (line) and F190N (adjacent continuum), and F212N (line) and F215N (continuum) respectively. The photometry of the central star and the nebular line emission is summarized in Table 3.

The largest source of uncertainty in our stellar photometry arises from the spatially variable attentuation and the complex, clumpy structure of the nebula. Near the CS, this structure varies on a scale as small as the radius of the first minimum in the PSF, so background estimation and subtraction are difficult. We found that the best NICMOS photometry is achieved by subtracting a scaled Pα line emission image from each of the images on which photometry is being performed. The scale factor is chosen to make the nebular background have a zero mean in the vicinity of the CS. (The Pα image is obtained by subtracting the F190N continuum image from the F187N Pα narrow band image, so that the central star is removed, leaving only the nebular line emission.) In this procedure we assume that the Pα line emission is a good tracer of total nebular line and continuum emission in the other NICMOS filters, at least in the region near the CS. We find that this method successfully removes the spatially variable nebular emission near the CS.

In the WFPC2 images the nebular surface brightness shows smaller variations relative to the CS. In this case we employ more conventional photometry and assume that the surface brightness

in an annulus immediately surrounding the CS is a fair representation of the background. The photometry was converted to flux density by applying the photometric calibration factor (PHOTFLAM) provided by STScI in the image header.

The CS photometry is dereddened using an attenuation value at the position of the CS of $A_V = 3.17$ mag. The Pα line emission photometry is corrected for an average nebular attenuation of $A_V = 2.97$ mag (Robberto et al. 1993). The correction at each wavelength is derived from the mean extinction curve given in Table 3.1 of Whittet (1992).

We calculate a hydrogen Zanstra temperature (cf. Osterbrock 1989) for each CS photometric value in Table 1, with the assumption of a blackbody CS spectrum. For the nebular line emission, we use the integrated Pα line flux given in Table 3. The greatest source of error in this calculation results from uncertainties in the nebular conditions on which the recombination coefficients depend. We adopt a nebular electron temperature of 15000 K and a nebular electron density of 10^4 cm^{-3} (cf. Roelfsma et al. 1991; Masson 1989), and use the corresponding Case B total recombination coefficient, α_B, and Pα emissivity calculated by Storey & Hummer (1995). The derived Zanstra temperatures of the CS are compiled in Table 3.

The derived CS temperatures are remarkably consistent (see Table 3). We find $T_* = 198,100 \pm 10,500$ K. Adopting a distance of 880±150 pc (Masson 1989), we find from the photometric data of Table 3 a mean CS luminosity of 7710 ± 860 $L_\odot$, and a photospheric radius of 5.21×10^9 cm. If we place the CS on the evolutionary tracks for hydrogen-burning post-AGB stars of Blöcker (1995), the CS lies very close to the theoretical track for an initial mass of 4 $M_\odot$ and a final core mass of 0.696 $M_\odot$. If this model is appropriate, the CS would have left the AGB only about 700 years ago. This timescale is consistent with the estimated age of 600 years for the ionized nebula (Masson 1989) based on the expansion velocity and size. The stellar evolutionary timescale is also comparable to the dynamical timescale of the H_2 lobes estimated in §4.1.2 above. Jaminet et al. (1991) have observed the neutral molecular envelope which surrounds the ionized gas and determined a mass of 1.4 (+0.8, –0.4) $M_\odot$. If the CS initial mass was in fact 4 $M_\odot$, and the final core mass is 0.7 $M_\odot$, then the star must have shed 3.3 $M_\odot$ over the course of its evolution. Of this amount, 40 – 50% was lost in the last 10^4 years, when the mass loss rate was some 1.5×10^{-4} $M_\odot$ yr^{-1} as inferred from models for the CO emission of the envelope (Jaminet et al. 1991). The balance of the mass loss might have occurred more slowly over a much longer time period, but the lack of clear observable signatures of this matter make it impossible to infer the rate or timescale of this earlier phase with any precision. The stellar properties found for NGC 7027 are summarized in Table 4.

5.2. Molecular Hydrogen Excitation and the Morphology of NGC 7027

The near-infrared spectrum of molecular hydrogen is the result of slow electric quadrapole transitions within the ground electronic state vibration-rotation levels. A possible excitation

mechanism likely in PNe is via the absorption of far-ultraviolet (FUV) photons in the Lyman and Werner bands of H_2. Upon absorption of a FUV photon, the molecule is left in an excited electronic state from which ≈10% of the decays out of that state result in transitions to the ground electronic state vibrational continuum and molecular dissociation occurs. Most often the molecule is left in an excited vibration-rotation level in the ground electronic state. The result is an identifiable near-IR fluorescence spectrum. This process is the primary way H_2 is destroyed, by photons and the peak in ro-vibrationally excited molecules defines the H_2 photo-dissociation region (PDR). In addition, the excitation of the near-IR H_2 spectrum can occur in regions with kinetic temperatures of $T_K \gtrsim 1000$ K and total densities $n_{tot} \gtrsim 10^4$ cm^{-3}. In PNe such temperatures are typically thought to be associated with shockwaves of moderate magnitude and over a limited range ($V_s \approx 5 - 50$ km s^{-1}; with the higher end of the range for C-type shocks only; Hollenbach & Shull 1977; Draine & Roberge 1982).

Graham et al. (1993a) argued, primarily from morphology, that the near-IR H_2 emission from NGC 7027 is caused by FUV excitation in the PDR. An analysis of near-IR spectra of NGC 7027 (Hora, Latter, & Deutsch 1999) confirms that hypothesis. There is no evidence of shock excitation, though localized shocked regions cannot be ruled out.

In a PDR the H_2 emission is observed in a thin transition region where the H_2 column density of FUV excited molecules peaks. Interior to the transition region the molecules have mostly been dissociated. Because the excitation process is by absorption of line photons, the depth of excitation is strongly limited by self-shielding of the molecules to Lyman and Werner band line radiation. The total extent of the transition region depends on molecular and total density, gas to dust ratio, and the strength and shape of the radiation field.

Comparison with quasi-steady state PDR models (Latter & Tielens, in preparation) finds that an observed average H_2 $v = 1 \rightarrow 0$ S(1) line brightness of 8.0×10^{-4} erg s^{-1} cm^{-2} ster^{-1} (§3.1) is consistent with a C-rich PDR exposed to a single star of temperature 200,000 K and a moderate total density of $n_{tot} \approx 5 \times 10^4$ cm^{-3}. The predicted $v = 2 - 1$ S(1) to $v = 1 - 0$ S(1) line ratio ranges from 0.12 to 0.06 and is nearly identical to that found by analysis of the H_2 spectrum (Hora, Latter, & Deutsch 1999). For a core mass of 0.696 $M_\odot$ and the observed H_2 line brightness, time dependent models of PDR evolution in PN suggest a PDR lifetime of $t \lesssim 1000$ years (Natta & Hollenbach 1998) consistent with estimates of the time since the object left the AGB (§5.1). The models are also consistent with a thin transition (H_2 emitting) region like that found from the 3-D models discussed in §4. The nonuniformity and patchiness of the transition region must be a result of structure in the circumstellar material itself. Instabilities of the type required are not understood in an interacting wind, photon-dominated environment. The "waves" present on the illuminated interior of the H_2 emission region resemble those seen in the HST/WFPC2 images of MyCn 18 (the "Etched Hourglass Nebula;" Sahai et al. 1999; Dayal et al. 1999), and although are seen in very different components of the gas (ionized versus molecular) most likely are a result of a similar instability.

It is important to consider whether the overall shape of the PDR (as it extends from the ionized core to the biconical, or bubble shaped H_2 emission) as found from our HST/NICMOS images is consistent with what is expected for an evolving PDR in a distribution of material likely to be present in a post-AGB circumstellar envelope. First, we must determine what is a likely distribution of circumstellar material. It has been known for some time that post-AGB objects and PNe generally do not have a spherical (radially symmetric) distribution of gas and dust. The most extreme examples include AFGL 2688 (the "Egg Nebula"), AFGL 618, M 2-9, and M 1-16 (to list just a few; see, e.g., Sahai et al. 1998; Latter et al. 1995; Latter et al. 1992; Hora & Latter 1994 and references therein). These objects have a predominantly axially symmetric distribution of circumstellar material such that the density is greatest at the equator and lowest near the two poles. With support from general morphological studies, hydrodynamic modeling, and polarimetric observations (e.g. Balick 1994; Trammell, Dinerstein & Goodrich 1994; Balick & Frank 1997) this type of distribution (to a widely varying degree) appears to be generally true for most, or all post-AGB objects. NGC 7027 is not an "extreme" bipolar nebula (of the type listed above), but we can assume that the equatorial to polar density contrast as the star evolved off the AGB has a functional form that goes roughly like $\sin(\Theta)$ with additional factors of order unity. Functions like this have been used to model the scattered light and molecular distribution from a number of bipolar PPNe and PNe (Yusef-Zadeh, Morris, & White 1984; Latter et al. 1992; Latter et al. 1993b).

In an environment with a single, central FUV source and with a constant gas to dust ratio, the dominant parameters that will determine the radial structure of the PDR are the density structure, $\rho(r)$ and the distance to the central source. For guidance some new computations were made using a code developed for a related purpose, and this topic will be explored quantitatively elsewhere (Latter & Tielens, in preparation). To first order, a PDR in a lower density region will have the ionized/neutral interface farther from the central source when compared to a higher density region. Similarly, the region of strongest H_2 FUV excitation will be farther out and have a somewhat larger linear extent than in a higher density region. This H/H_2 interface region will approximately follow iso-column density contours at $\sim 4 \times 10^{21}$ cm^{-2} or $A_V \approx 2$ magnitudes. Details will depend strongly on the exact distribution of material. But, it is evident that an axially symmetric distribution of circumstellar material of the type discussed above will produce a PDR morphology like that observed in NGC 7027. More specifically, it is expected to be an ellipsoidal or bipolar H^+/H° interface, surrounded by a bipolar bubble structure defining the H/H_2 interface and revealed in FUV excited H_2 emission – like that modeled here. Somewhat farther out, the C/CO interface region is, as shown by the data of Graham et al. 1993a, consistent with that found for the inner regions. The morphological evolution of the H^+/H° interface region and the ionized core is not predicted by strict PDR evolution alone. The internal density structure appears to have equilibrated in the shell and cavity (§4.2) because the sound crossing time is much shorter than the expansion timescale. The outward motion of this interface will be faster in the lower density polar regions, magnifying the asymmetric shape. If the star is on the cooling track, then the ionization front might better be described as a "recombination" front as the number of ionizing

photons goes down (Schoenberner 1999, personal communication).

Nested hourglass shapes and ellipsoids are predicted by numerical hydrodynamical simulations (such as Mellema & Frank 1995; Icke 1988), but for interaction speeds much higher than so far seen in NGC 7027. In addition, the molecular hydrogen emission from NGC 7027 is from a strong PDR, not a shocked wind interface. There is similarity in the overall morphology of the PDR, including the ionized core in NGC 7027 to emission morphologies predicted in strong interacting winds starting in an axisymmetric density distribution. Because of this apparent similarity, a full description of the observed structure and its evolution requires coupled time-dependent PDR and hydrodynamic modeling. When combined with detailed chemical modeling of the neutral regions, the data presented here can be used to determine the exact density distribution of the circumstellar envelope.

6. Discussion

6.1. Previous Kinematic Results

In a detailed multiwavelength study, Graham et al. (1993a) found that uniform, radial expansion of a prolate spheroid, tilted to the line of sight is consistent with the millimeter-wave (CO) position-velocity maps. However the CO P-V diagram differs from the H_2 P-V diagram presented here. This is not unexpected since the observed emission from the two molecules is produced under very different excitation conditions. Therefore the two molecules trace different spatial/kinematical structures. Observations have been made with the "BEAR" instrument (a 256×256 pixel HgCdTe camera coupled to a Fourier transform spectrometer, with a spectral resolution $\approx$ 52.2 km s^{-1}) on the Canada-France-Hawaii Telescope (Cox et al. 1997). Cox et al. found that the velocity field appeared to them as an equatorial "torus" suggests that north pole is tilted away from observer. This result is inconsistent with our interpretation of the HST images, our 3-D modeling of those images, and the higher spectral resolution CSHELL data. The high spatial resolution and sensitivity of the HST images shows that the front part of the top rim lies in front of the the ionized nebula (not behind), suggesting that the top (northern side) is tilted *toward* the observer. We cannot resolve this discrepancy with the data available. We suggest that the spectral resolution available to Cox et al. (1997) was not sufficent to fully deconvolve the subtle, but complex velocity structure that must be present (Kelly et al. 1999). In addition, the model schematic given by Jaminet et al. (1991) shows the same orientation as Cox et al. (north pole away) for the fast molecular wind traced by CO $J = 3 \rightarrow 2$ line emission, which presumably has a similar flow direction as the ionized gas. It is entirely possible that the flow along the back of the cone (or bubble) has been confused with a flow along the polar axis, which in our model would not be the dominant emitting region. Bains et al. (1997) found from their high spectral resolution radio and optical observations, an orientation for NGC 7027 that is consistent with ours: i.e. that the NE lobe is blue-shifted, SW lobe is red-shifted.

6.2. Evolution of the PDR in NGC 7027

A full modeling of PDR evolution is beyond the scope of this paper. We can, however, make an assessment of such PDR evolution based on available models. The morphological evolution of the PDR will depend most strongly on the distribution of material in the circumstellar envelope. For NGC 7027 the post-AGB circumstellar envelope must have been axially symmetric with a gradual decrease in density from the equatorial region to the poles. A dense equatorial disk cannot be ruled out, but there is no evidence in these data, or other molecular data (Bieging, Wilner, & Thronson 1991; Jaminet et al. 1991; Graham et al. 1993a), that requires or even suggests one. For that reason, we consider such a structure as unlikely to be present. The density distribution appears typical for other post-AGB objects with an equatorial to polar density contrast of $\sim 2 - 10$, such that it is not as great as the extreme bipolar proto-PNe (see §5.2). In much less than the cooling timescale of the central star, the PDR will be established quickly in all directions, with the fastest evolution in the polar regions. The result will most likely be for NGC 7027 to become a butterfly-type nebula similar in gross properties to (e.g.) NGC 2346. Wind interactions for this type of morphological evolution are not required.

The timescale for PDR evolution is highly uncertain (other timescales are discussed in §5.1), but reasonable estimates can, and have been made (see, e.g., Tielens 1993). It is straightforward to show that for a constant mass loss rate and parameters typical of high mass loss rate carbon stars, the timescale for a PDR to completely move through the circumstellar envelope can be estimated by integrating the equations of molecular formation and destruction with respect to radius and time, as was done by Tielens 1993. For a constant wind velocity $V_w = 20$ km s^{-1}, a constant mass loss rate $\dot{M} = 10^{-4}$ M$_\odot$ yr^{-1}, and a stellar luminosity $L_* = 6000$ L$_\odot$, it can be shown that the dissociation front travels a distance $r_i \approx 3 \times 10^{16}$ cm in $t_i \approx 65$ years with a PDR speed of $V_i \approx 263$ km s^{-1} (see Tielens 1993 for a more detailed discussion; see also Natta & Hollenbach 1998). Tielens suggested clumping as how the evolution is slowed in real nebulae. Although widespread clumping and structure is seen in these data, it does not appear at the size scales required, or marginally so at best ($R \gtrsim 10^{16}$ cm and $A_V \gtrsim 4$ mag). Even if clumping is important in localized regions, it is more likely that we now know several of the assumptions used to derive this evolutionary timescale are not valid, and if properly accounted for will tend to increase the timescale. The mass loss rate is not constant. The "ring" structure clearly visible in AFGL 2688 (Latter et al. 1993b; Sahai et al. 1998) indicates a time varying mass loss rate on a timescale of hundreds of years. The same type of structures are seen in other objects observed (Kwok et al. 1998), including NGC 7027 (see, e.g., Bond et al. 1997). In addition, the distribution of material is not spherical. The degree to which the mass loss rate is varying is not known. Nor is how a non-spherical distribution of attenuating and shielding material will alter the evolutionary timescales (see, however, Natta & Hollenbach 1998). Additional work must be done to characterize these properties and how they relate to evolution. From the above expression and an assessment of the impact of uncertain parameters, it seems likely that the timescale for NGC 7027 to evolve away from its current state will be only a few hundred to a few thousand years (see also Natta &

Hollenbach 1998). Wind interactions will complicate the picture by adding hydrodynamic effects and changes to the density structure. However, evolution to the current epoch appears to be described fully by the interaction of FUV and ionizing photons with an AGB wind that has (or had) a somewhat enhanced mass loss rate in the equatorial plane. While there is evidence for recent jet interactions with the outflow, the jets have not dominated the morphological shaping. It is worth monitoring NGC 7027 at very high spatial resolution for morphological changes caused by jets and UV photons over the next several decades.

7. Summary

The HST/NICMOS observations presented in this paper reveal the detailed structure and morphology of the young planetary nebula NGC 7027 with unprecedented clarity. The molecular photodissociation region is found to be of an apparently different overall structure from that of the ionized core. We have constructed 3-dimensional, axisymmetric models for the morphology of NGC 7027 based on these NICMOS near-infrared data and HST archive visible light data. The object can be well described by three distinct components: an ellipsoidal shell that is the ionized core, a bipolar hourglass structure outside the ionized core that is the excited molecular hydrogen region (or the photodissociation region), and a nearly spherical outer region seen in dust scattered light and is the cool, neutral molecular envelope. It is argued that such a structure is consistent with one which would be produced by a photodissociation region with a central source of far-ultraviolet photons surrounded by an axisymmetric distribution of gas and dust that has a decreasing total density with increasing angle toward the polar regions of the system.

The central star is clearly revealed by these data. We are able to determine the most accurate value for the temperature of the star $T_* = 198,100 \pm 10,500$ K with a luminosity of $L_* \approx 7,700$ $L_\odot$. From various indicators, including the central star timescale, dynamical timescale, and timescale for evolution of the photodissocation region, we conclude that NGC 7027 left the asymptotic giant branch 700 to 1000 years ago. For such rapid evolution, it is likely that objects like NGC 7027 do not go through a proto-planetary nebula phase that is longer than a few tens of years, and as such would be nearly undetectable during such a brief phase.

There is strong evidence for one, and possibly two highly collimated bipolar jets in NGC 7027. The jets themselves are not seen with the present data, but the disturbance caused by them is clearly visible. It is possible that this jet, or jets have shut off during the current epoch of evolution. Such jets have been seen in other planetary nebulae, but NGC 7027 might be the youngest in terms of evolution. There are nonuniformities and wave-like structures seen in these data that must be caused by poorly understood instabilities in the outflowing wind.

We conclude that while wind interactions will be important to the future evolution of NGC 7027, it is the evolution of the PDR, as the central star dissociates, then ionizes, the circumstellar medium, that will dominate the apparent morphological evolution of this object. This is in

contrast to the idea that interacting winds always dominate the evolution and shaping of planetary nebulae. Evolution driven by far-ultraviolet photons might be more common in planetary nebulae than has been previously thought (see, e.g., Hora, Latter, & Deutsch 1999). Such photon-driven evolution will be more important in objects with higher mass central stars (and therefore high luminosity, temperature, and UV flux), than in those with low mass stars. But, it is the high mass objects that also have the higher density molecular envelopes ejected during a high mass loss rate phase on the asymptotic giant branch, and as such will show the strongest emission from a photodissociation region. NGC 7027 is perhaps the most extreme example known at this time, but it is not unique – except for the important and very brief moment in evolution at which we have found it.

This work is dedicated to the memory of Christopher Skinner, our Contact Scientist at STScI, our colleague, and our friend. We miss his support, comments, and criticism. He challenged us to search for the truth, and through that he enriched us all.

We gratefully thank the members of the NICMOS Instrument Development Team at the University of Arizona for help, suggestions, comments, and data; especially Marcia Rieke, Dean Hines, and Rodger Thompson. We also thank Sun Kwok and Nancy Silbermann for useful conversations, and Tom Soifer for reading the manuscript. Support for this work was provided by NASA through grant number GO-7365-01 from the Space Telescope Science Institute, which is operated by AURA, Inc., under NASA contract NAS5-26555. W.B.L. and J.L.H. acknowledge additional support from NASA grant 399-20-61 from the Long Term Space Astrophysics Program.

REFERENCES

Atherton, P. D., Hicks, T. R., Reay, N. K., Robinson, G. J., Worswick, S. P., & Phillips, J. P. 1979, ApJ, 232, 786

Bains, I., Bryce, M., Pedlar, A., Muxlow, T. W. B., Thomasson, P. & Mellema, G. 1997, IAU Symposium 180 Planetary Nebulae, Eds. H.J. Habing & H.J.G.L.M. Lamers, (Dordrecht : Kluwer), 206

Balick, B. 1994, Ap&SS, 216, 13

Balick, B. & Frank, A. 1997, IAU Symposium 180, Planetary Nebulae, Eds. H.J. Habing & H.J.G.L.M. Lamers, (Dordrecht : Kluwer), 190

Bieging, J. H., Wilner, D., & Thronson, H. A. 1991, ApJ, 379, 271

Blöcker, T. 1995, AA, 299, 755

Bond, H. E., Fullton, L. K., Schaefer, K. G., Ciardullo, R., & Sipior, M. 1997, IAU Symposium 180, Planetary Nebulae, Eds. H.J. Habing & H.J.G.L.M. Lamers, (Dordrecht : Kluwer), 211

Cox, P., Maillard, J.-P., Huggins, P. J., Forveille, T., Simons, D., Guiloteau, S. Riguat, F., Bachiller, R., & Omont, A. 1997, A&A, 321, 907

Corradi, R. L. M., & Schwarz, H. E. 1995, A&A, 293, 871

Dayal, A., Sahai, R., Watson, A. M., Trauger, J. T., Burrows, C. J., Stapelfeldt, K. R., & Gallagher, J. S. 1999, AJ, submitted

Dinerstein, H. L., Sneden, C., & Uglum, J. 1995, ApJ, 447, 262

Draine, B. T., & Roberge, W. T. 1982, ApJ, 259, L91

Ferland, G. 1997, HAZY, a Brief Introduction to Cloudy, University of Kentucky Internal Report

Graham, J. R., Serabyn, E., Herbst, T. M., Matthews, K., Neugebauer, G., Soifer, B. T., Wilson, T. D., & Beckwith, S. 1993a, AJ, 105, 250

Graham, J. R., Herbst, T. M., Matthews, K., Neugebauer, G., Soifer, B. T., Serabyn, E., & Beckwith, S. 1993b, ApJ, 408, L105

Heap, S., & Hintzen, P. 1990, ApJ, 353, 200

Hollenbach, D. J., & Shull, J. M. 1977, ApJ, 216, 419

Hollenbach, D. J., & Tielens, A. G. G. M. 1997, ARA&A, 35, 179

Hora, J. L., & Latter, W. B. 1994, ApJ, 437, 281

Hora, J. L., Latter, W. B. & Deutsch, L. K. 1999, ApJS, 124, 195

Huggins, P. J., & Healy, A. P. 1989, ApJ; 345, 201

Huggins, P. J., Bachiller, R., Cox, P., & Forveille, T. 1996, A&A, 315, 284

Icke, V. 1988, A&A, 202, 177

Jacoby, G. 1988, ApJ, 333, 193

Jaminet, P. A., Danchi, W. C., Sutton, E. C., Russell, A. P. G., Sandell, G., Bieging, J. H., & Wilner, D. 1991, ApJ, 380, 461

Kastner, J. H., Gatley, I., Merrill, K. M., Probst, R., & Weintraub, D. A. 1994, ApJ, 421, 600

Kastner, J. H., Weintraub, D. A., Gatley, I., Merrill, K. M., & Probst, R. 1996, ApJ, 462, 777

Kelly, D. M., et al. 1999, ApJ, in preparation.

Kwok, S., Su, K. Y. L., Hrivnak, B. J., Sahai, R. & Dayal, A. 1998, BAAS, 30, 1273.

Lame, N. J., Harrington, J. P. & Borkowski, K. 1997, IAU Symposium 180, Planetary Nebulae, (Dordrecht: Kluwer Academic Publishers), p. 252

Latter, W.B., Kelly, D. M., Hora, J. L., & Deutsch, L. K. 1995, ApJS, 100, 159

Latter, W. B., Walker, C. K., & Maloney, P. R. 1993, ApJ, 419, L97

Latter, W. B., Hora, J. L., Kelly, D. M., Deutsch, L. K., & Maloney, P. R. 1993, AJ, 106, 260

Latter, W. B., Maloney, P. R., Kelly, D. M., Black, J. H., Rieke, G. H., & Rieke, M. J. 1992, ApJ, 389, 347

Lopez, J. A., Meaburn, J., Bryce, M. & Holloway, A. J. 1998, ApJ, 493, 803

Martin, P. G. & Rogers, C. 1987, ApJ, 322, 374

Masson, C.R. 1989, ApJ, 336, 294

Mellema, G., & Frank, A. 1995, MNRAS, 273, 401

Natta, A., & Hollenbach, D. 1998, A&A, 337, 517

Osterbrock, D. E. 1989, Astrophysics of Gaseous Nebulae and Active Galactic Nucleii, (University Science Books: Mill Valley)

Robberto, M., Clampin, M., Ligori, S., Paresce, F., & Staude, H.J. 1993, A&A, 280, 241

Roelfsema, P. R., Goss, W. M., Pottasch, S. R., & Zijlstra, A. 1991, A&A, 251, 611

Sahai, R., et al. 1998, ApJ, 493, 301

Sahai, R., et al. 1999, AJ, in press

Sauval, A. J. & Tatum, J. B. 1984, ApJS, 56, 193

Sternberg, A., & Dalgarno, A. 1989, ApJ, 338, 197

Storey, P.J., & Hummer, D.G. 1995, MNRAS, 272, 41

Tielens, A. G. G. M. 1993, in IAU Symp. 155, Planetary Nebulae, ed. R. Weinberger and A. Acker (Dordrecht: Reidel), 155

Tielens, A. G. G. M., & Hollenbach, D. 1985, ApJ291, 722

Trammell, S. R., Dinerstein, H. L., & Goodrich, R. W. 1993, ApJ, 402, 249

Trammell, S. R., Dinerstein, H. L. & Goodrich, R. W. 1994, AJ, 108, 984

Volk, K., & Kwok, S. 1997, ApJ, 477, 722

Whittet, D.C.B. 1992, Dust in the Galactic Environment (Bristol: Inst. of Physics Publ.), p. 67

Wolniewiez, L., Simbotin, I., & Dalgarno, A. 1998, ApJS, 115, 293

Woodward, C. E., Pipher, J. L., Forrest, W. J., Moneti, A., & Shure, M. A. 1992, ApJ, 385, 567

Yusef-Zadeh, F., Morris, M., & White, R. L. 1984, ApJ, 278, 186

Zuckerman, B., & Gatley, I. 1988, ApJ, 324, 501

This preprint was prepared with the AAS LaTeX macros v4.0.

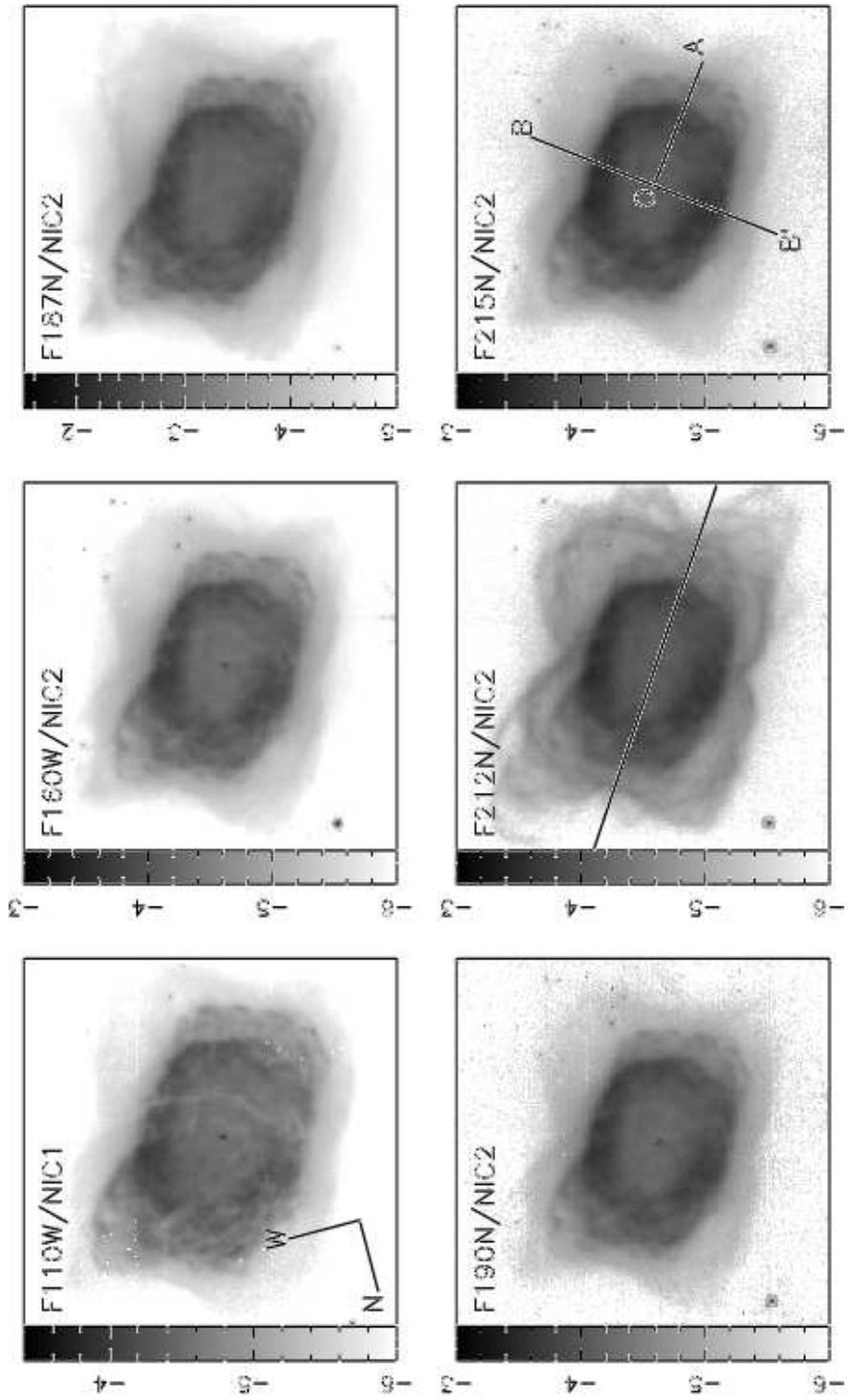

Fig. 1.— NICMOS/HST mosaiced images of NGC 7027 covering 1.10 μm to 2.15 μm. The F110W/NIC1 image has a pixel scale of 0.043″ pixel^{-1} and a field of view of 16″×16″; the other images have a scale of 0.075″ pixel^{-1} and a field of view of 19.2″×19.2″. The images are in units of Jy pixel^{-1}, and are displayed here using a logarithmic stretch. The orientation of the CSHELL slit is shown in 1(e) and 1(f) shows directions for the radial cuts in Fig. 7.

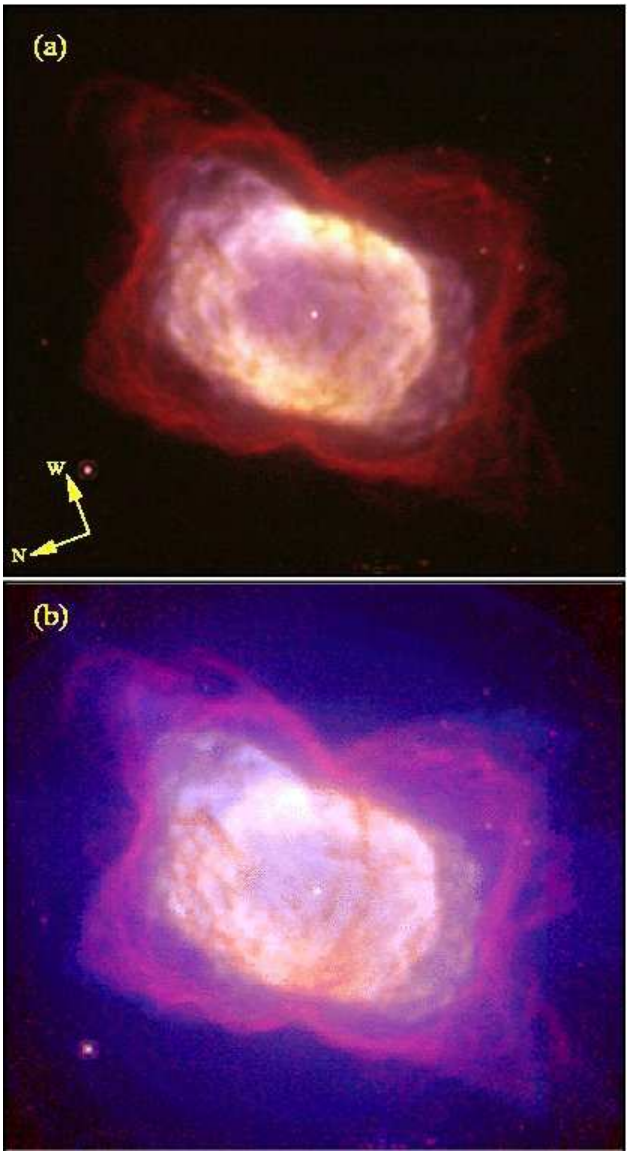

Fig. 2.— *(a)* Three–color composite of data taken in three NICMOS filters. Red is F212N (molecular hydrogen), green is F215N (continuum), and blue is F110W (continuum). These data have been highly stretched for visualization and the relative brightness between bands has not been maintained. It is evident from this image that the dark "ring" going across the bright core, is glowing in λ=2.121 μm molecular hydrogen emission (seen in red/orange color) that is contiguous with the more extended emission. When compared with the individual filter images (Fig. 1), it is clear that there is a strong correlation between the H_2 emission and regions of high attenuation. *(b)* Three-color composite of two NICMOS images and one acquired with WFPC2. Red is NICMOS F212N, green is NICMOS F190N (continuum), and blue is WFPC2 V and I bands combined. As with the images in *(a)* (NICMOS), the combined data has been highly stretched for visualization. Many of the same features seen in *(a)* are visible here as well. Dust scattered visible light is seen in these data as the extended blue emission.

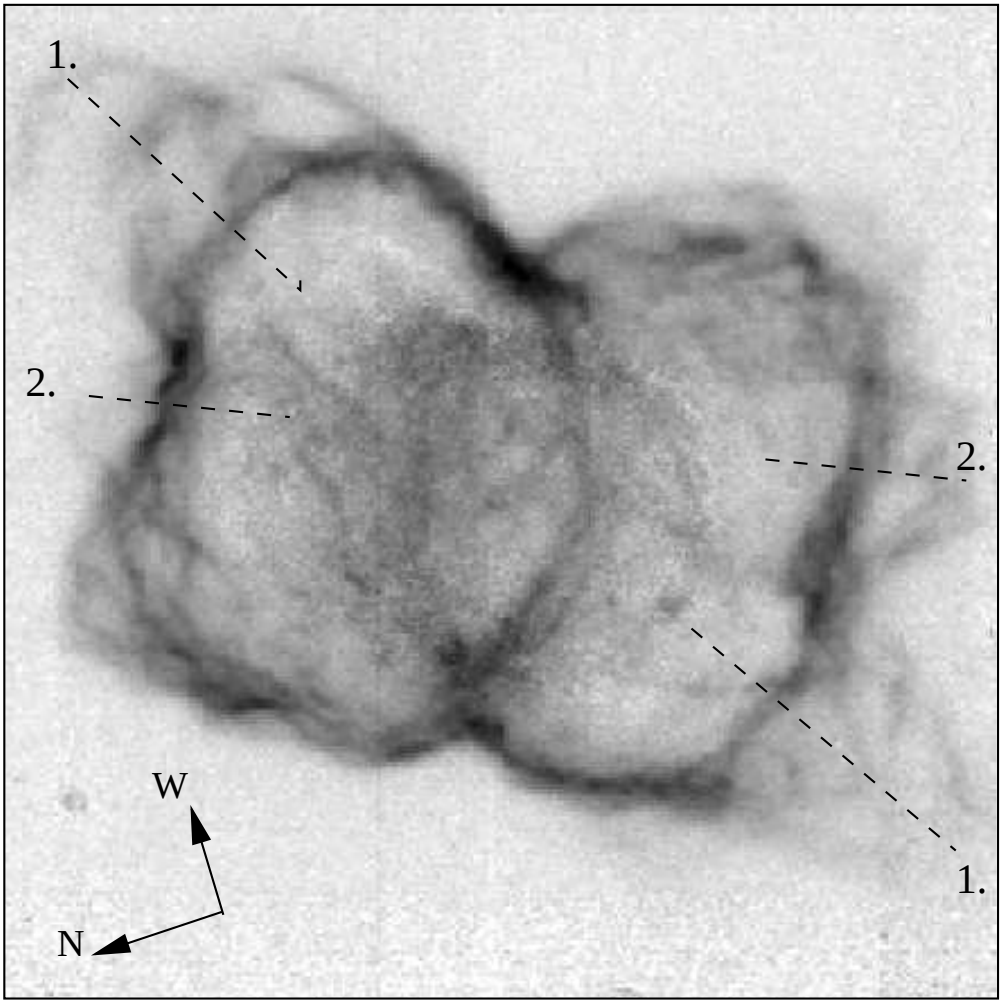

Fig. 3.— Continuum-subtracted H_2 image. The two intersecting rings are interpreted as the edges of a tilted bicone (see text). Two outflows/jets, labelled 1 and 2, appear to have disturbed the general morphology. Field of View is $\sim 20'' \times 20''$.

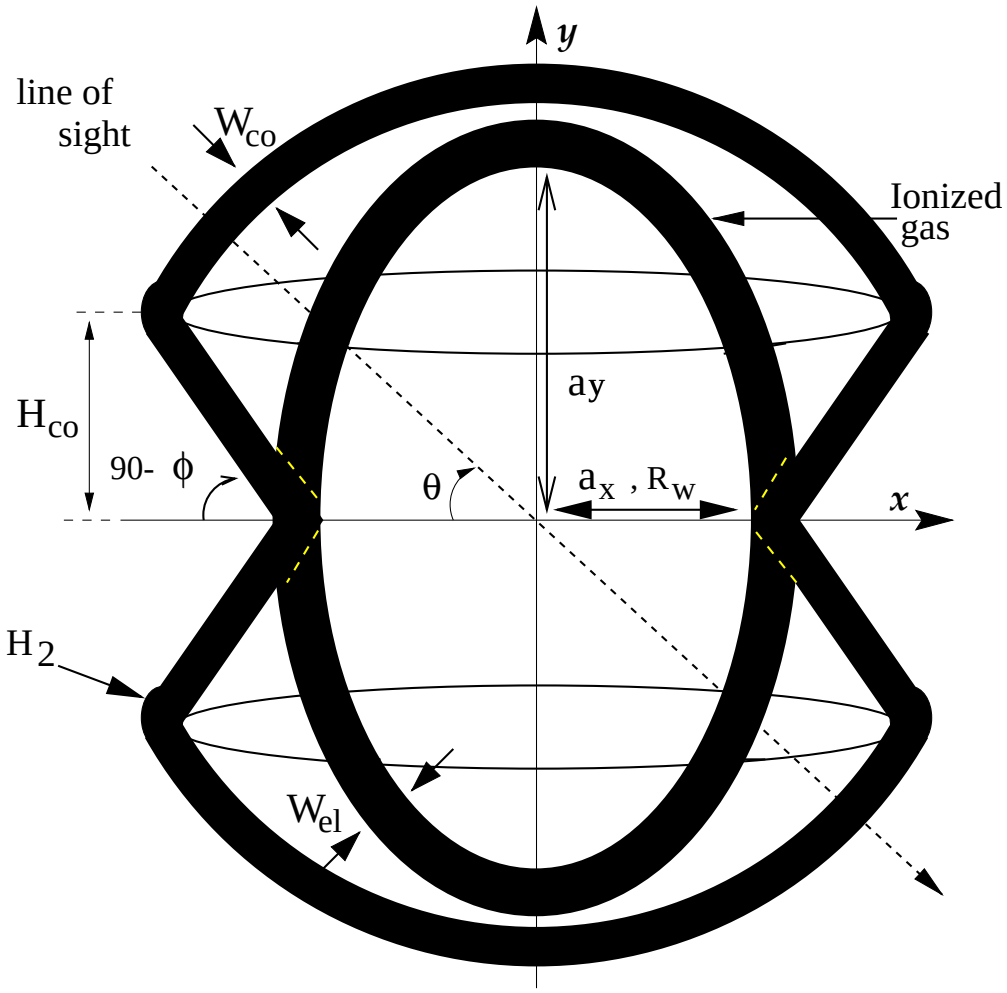

Fig. 4.— A schematic of the 2–component axially symmetric model. The bicone and the ellipsoid share the same inner radius in the equatorial (X-Z) plane, i.e. $a_x = R_w$ (see text for details). The widths of both components, W_{co}, W_{el}, are derived independently but assumed to be constant. θ is the tilt of the nebula to the line of sight, ϕ is the semi-opening angle of the bicone, H_{co} is the semi-height of the cone and a_x, a_y and a_z are the semi-axes of the ellipsoid. Both of the "caps" are sections of a sphere centered at the origin.

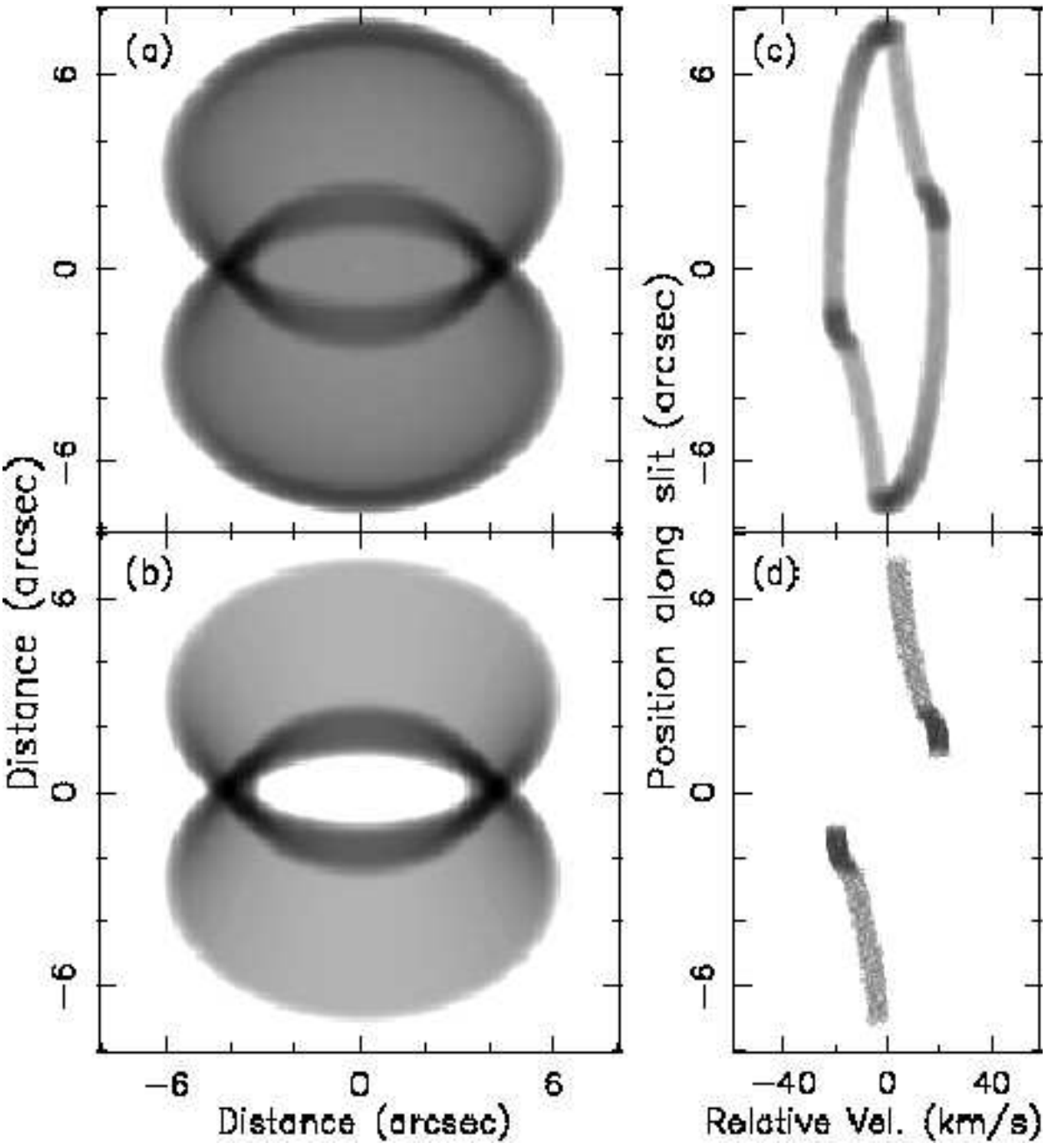

Fig. 5.— Bicone model images and Position–Velocity diagrams obtained by placing a slit along the long axis of the nebula. *(a), (c)*: "Best-fit" model bicone with "cap"; *(b), (d)*: bicone without "cap".

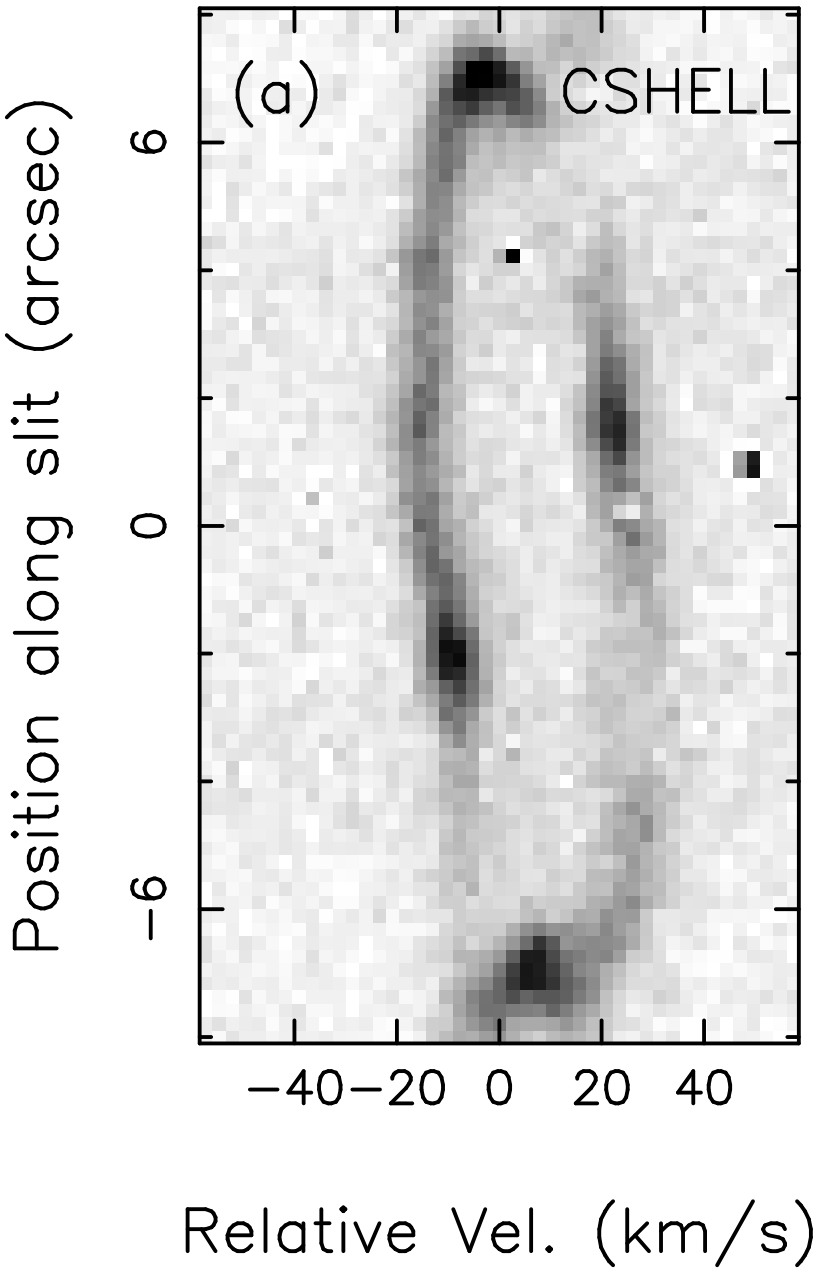
(a)
CSHELL
Position along slit (arcsec)
6
0
−6
−40
−20
0
20
40
Relative Vel. (km/s)

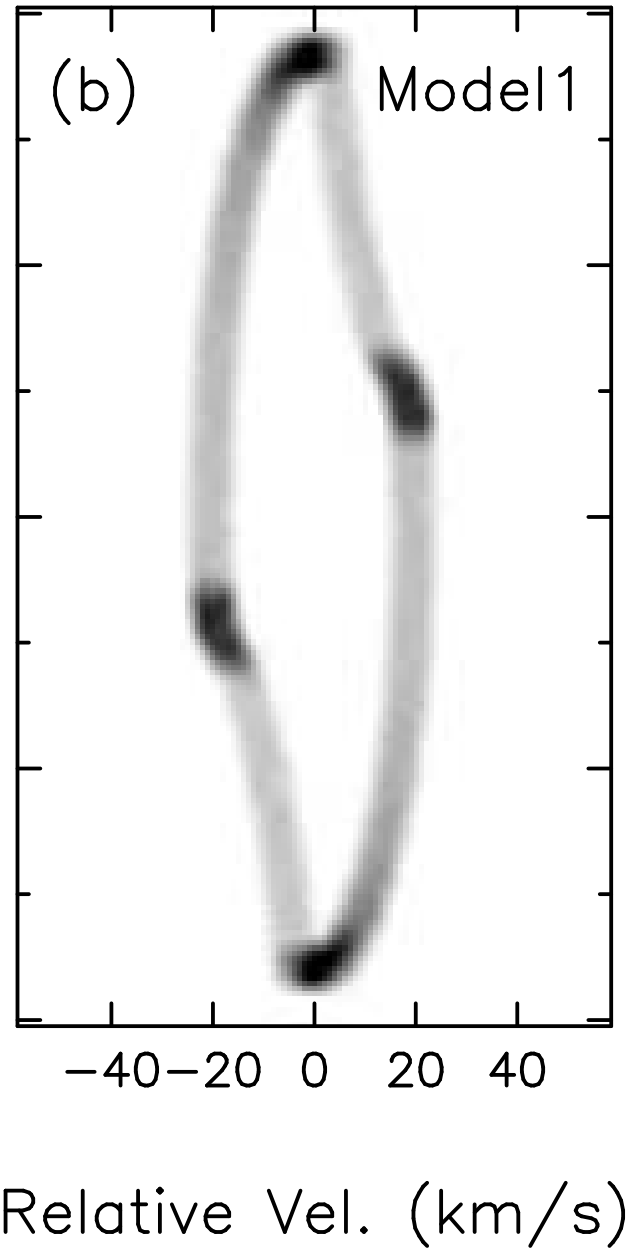
(b)
Model1
−40
−20
0
20
40
Relative Vel. (km/s)

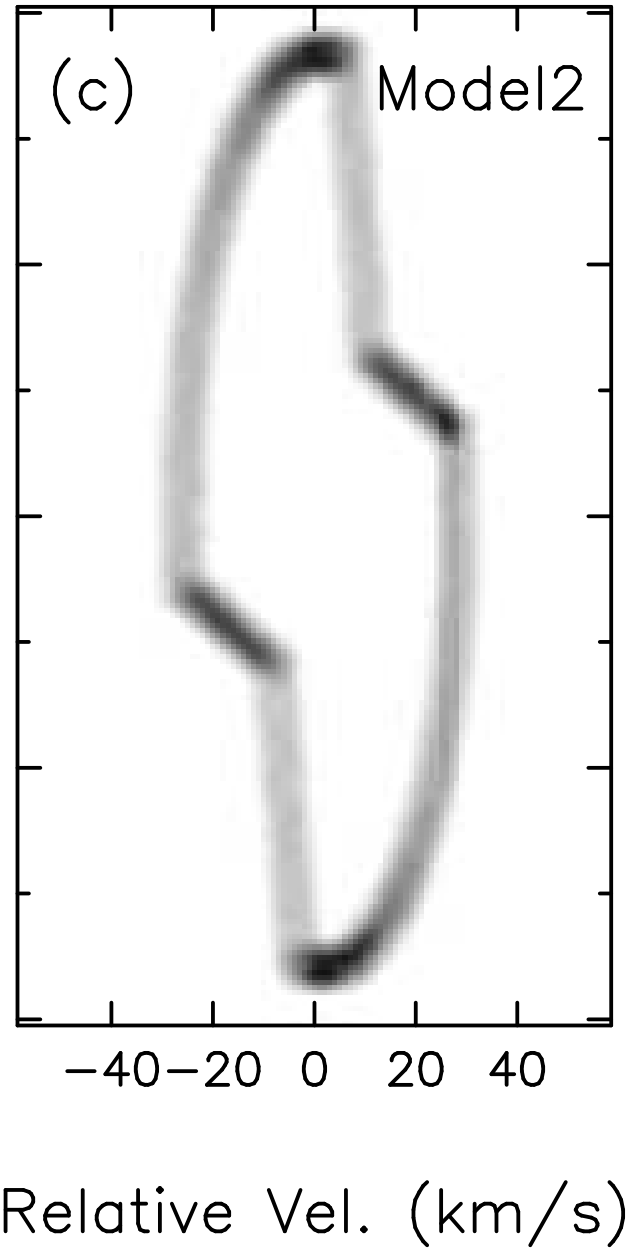

Fig. 6.— Observed Position–Velocity diagram obtained by placing the CSHELL slit along the major axis of NGC 7027 (see Fig. 1(e)), compared with model P-V diagrams, shown on the same spatial/velocity scale. *(a)* The CSHELL observations have a velocity scale of $2.6''$ pixel^{-1}. *(b)* Best-fit model with a constant velocity, V = 20 km s^{-1}. *(c)* Model with varying velocity, V $\propto$ R$^{1.0}$ km s^{-1}.

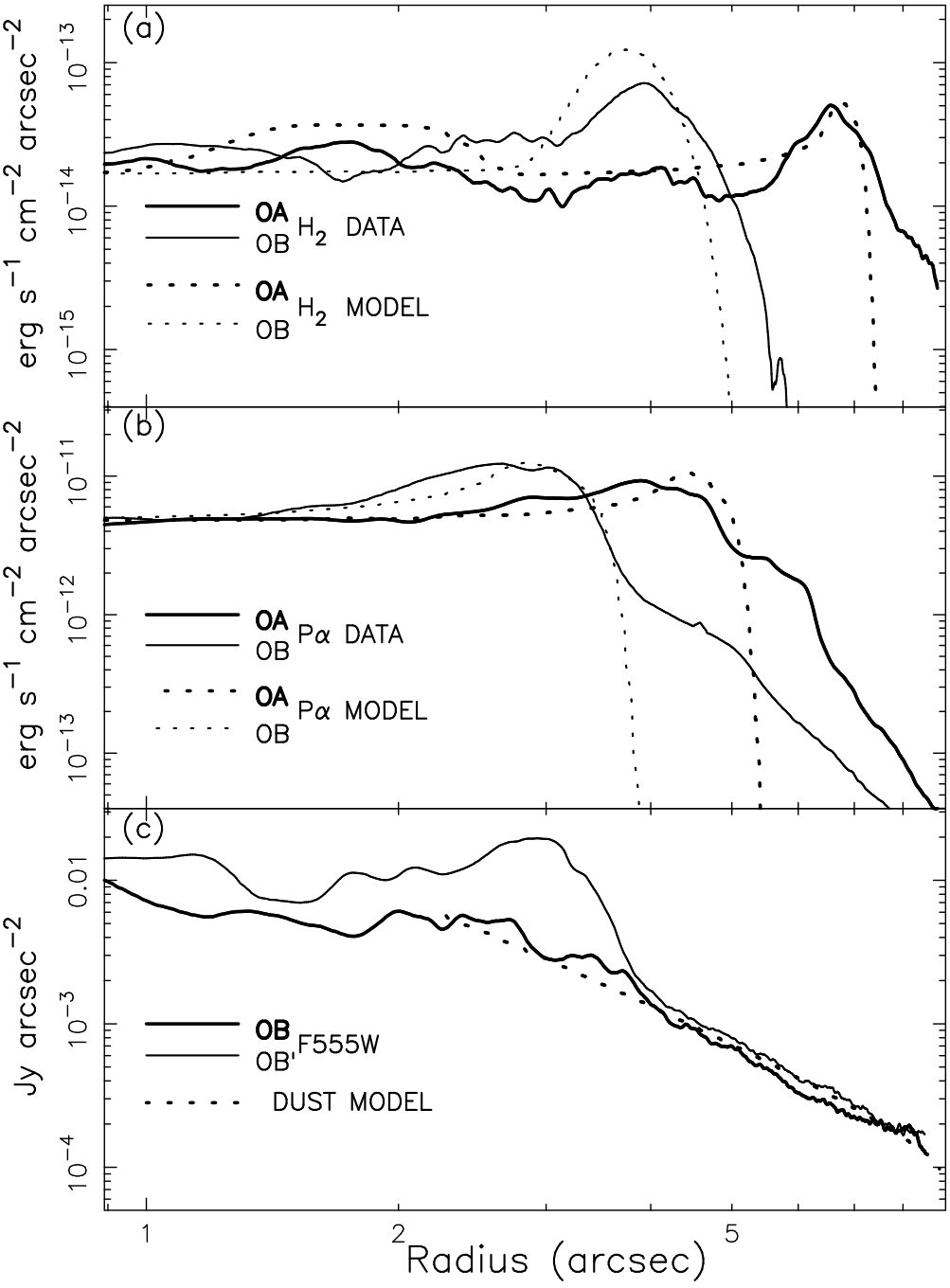

Fig. 7.— Radial cuts across images. The direction of the cuts (OA, OB, OA') are shown in Fig. 1, F215N panel. *(a)*: Radial cuts across the continuum subtracted H_2 image and the H_2 bicone model. Dark solid line is a cut along the major axis, faint solid line is a cut along the minor axis. The dotted lines are corresponding radial cuts through the bicone model. *(b)*: Radial cuts across the continuum subtracted Pα image and the constant–density ellipsoid model. Dark solid line is a cut along the major axis, faint solid line is a cut along the minor axis. The dotted lines are corresponding radial cuts through the ellipsoid model. *(c)*: Radial cuts along the minor axis of the F555W image (solid lines) overlayed on a radial cut from the optically thin, uniform, spherical model of scattering dust grains.

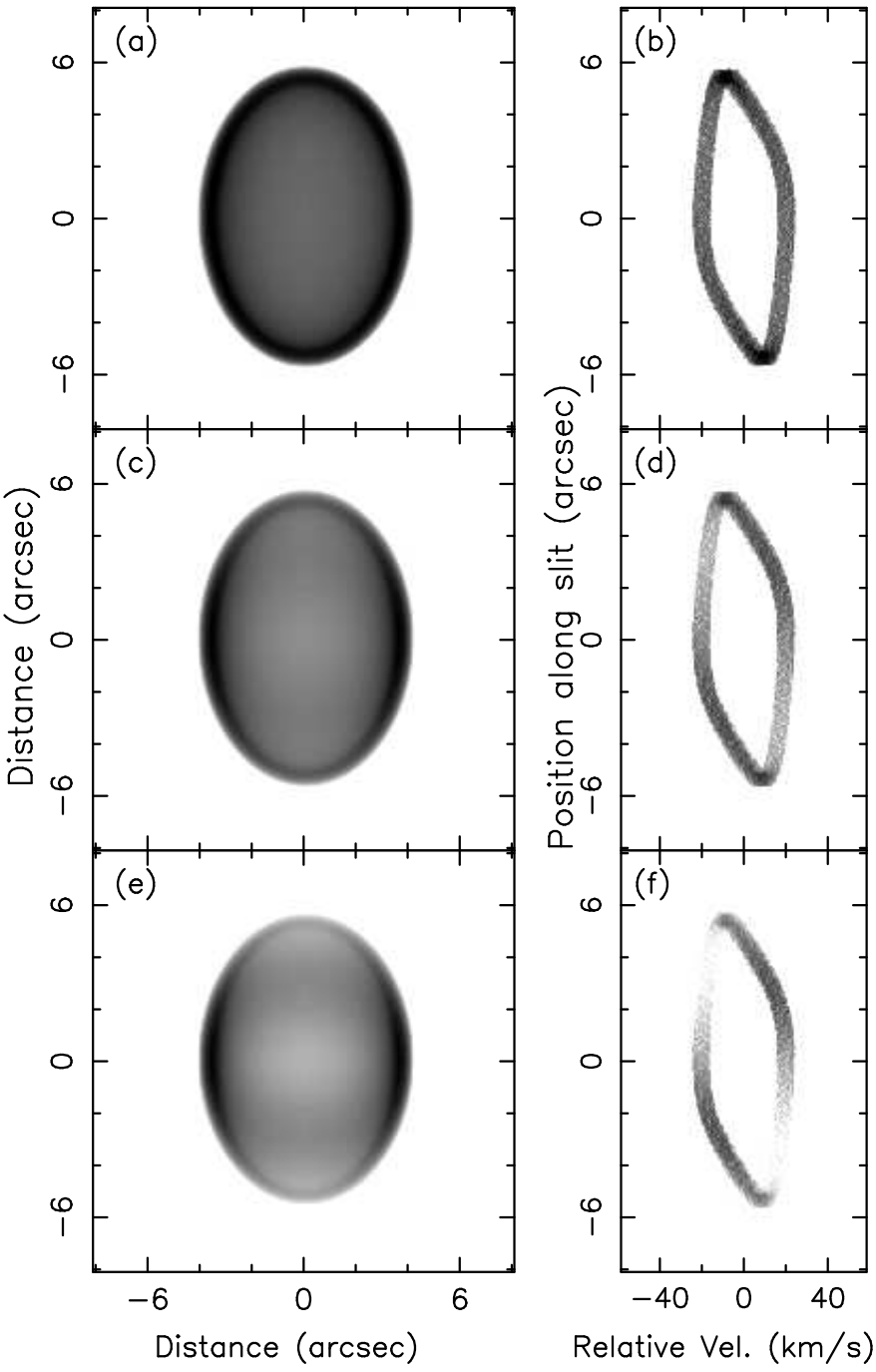

Fig. 8.— Ellipsoidal shell models – Images and Position–Velocity diagrams for the distribution of ionized gas. In each model the velocity is assumed to be constant. *(a), (b)*: Constant density; *(c), (d)*: Density $\propto R^{-1}$; *(e), (f)*: Density $\propto R^{-2}$. The equator–to–pole intensity contrasts in the models with decreasing density are much higher than the observed intensity contrast, suggesting that density changes by $\lesssim 20\%$ – 30% going from the equator to pole.

Table 1. Summary of Observations

Camera	Filter	λ_{eff} (μm)	$\Delta\lambda_{eff}$ (μm)	Integration Time (s)
NIC1	110W	1.1022	0.5920	256
NIC2	160W	1.5931	0.4030	256
NIC2	187N	1.8738	0.0192	1024
NIC2	190N	1.9003	0.0174	1024
NIC2	205W	2.0406	0.6125	1024
NIC2	212N	2.121	0.021	2560
NIC2	215N	2.149	0.020	2176

Table 2. Model Parameters for NGC 7027

Component	Shape	Tilt	Parameters[a]			
H_2	Bicone	45^0	ϕ[b]	R_w[b]	H_{co}[b]	Width (W_{co})
			30^0	$2.8''$	$3.9''$	$0.5''$
Ionized Gas	Ellipsoid	45^0	a_x	a_y	a_z	Width (W_{el})
			$2.8''$	$5.3''$	$2.8''$	$0.9''$
Cool dust	Sphere	–	R_{in}	R_{out}		
			$3.0''$	$8.0''$		

[a]Dimensions given in arcsec. At the adopted distance of 880 pc, $1''$=1.32×10^{16} cm.

[b]ϕ is the semi opening–angle of the cone, R_w is the radius of the waist of the cone and H_{co} is the semi-height of the cone.

Table 3. Photometry and Zanstra Temperature

Filter	Description	Stellar Photometry		Nebular Photometry		T_Z
		$F_{\nu,obs}$ (mJy)	$F_{\nu,0}$[a] (mJy)	$F_{\nu,obs}$ (mJy)	$F_{\nu,0}$[a] (mJy)	(K)
F205W	continuum	1.197±0.06	1.68±0.10	2.776±0.14	3.739±0.40	192,000±7,700
F190N	Pα cont.	1.308±0.07	1.88±0.11	1.36±0.01	1.91 ± 0.08	190,000±8,600
F160W	continuum	1.377±0.07	2.30±0.18	1.082±0.05	1.693±0.19	207,000±8,300
F110W	continuum	1.765±0.09	5.98±0.57	1.394±0.07	3.671±0.56	198,500±8,900
F814W[b]	continuum	1.362±0.14	7.78±1.44	0.875±0.09	4.464±0.60	214,000±18,200
F555W[c]	continuum	0.977±0.10	25.03±6.38	0.922±0.09	14.214±2.27	187,300±20,600
F187N	Pα line+cont.	———	———	24.64±0.62	34.81 ± 1.39	———
F212N[d]	H_2 line+cont.	———	———	1.92±0.05	2.53 ± 0.09	———
F215N[d]	H_2 cont.	———	———	1.81±0.05	2.36 ± 0.08	———

[a]The flux density has been corrected for attenuation using the mean extinction curve in Table 3.1 of Whittet (1992), and $A_V = 3.17$ mag for the CS and 2.97 mag for mean nebular attenuation (Robberto et al. 1993).

[b]Images taken by the WFPC2/HST, extracted from the HST archive. $\lambda_{eff} = 0.811\mu$m; $\Delta\lambda = 0.176\mu$m

[c]Images taken by the WFPC2/HST, extracted from the HST archive. $\lambda_{eff} = 0.513\mu$m; $\Delta\lambda = 0.122\mu$m

[d]The F212N filter is contaminated by He I and the F215N filter by Brγ. See §3.1.1 for a discussion.

Table 4. Derived Properties of the Central Star

Stellar Property	Value
Zanstra temperature	198,100 ± 10,500 K
Luminosity[a]	7,710 ± 860 $L_\odot$
Radius	5.21 $\times 10^9$ cm
Core mass[b]	0.7 $M_\odot$
Initial mass[b]	4 $M_\odot$
Evolutionary timescale	700 y

[a]Based on best fit stellar temperature and a distance of 880 pc.

[b]From evolutionary tracks of Blöcker (1995).